Title

The Role of Southeast Asian Island Topography on Indo-Pacific Climate and Silicate Weathering

Journal

Paleoceanography and Paleoclimatology, 39(3)

ISSN

2572-4517

Authors

Chiang, John CH

Maffre, Pierre

Swanson-Hysell, Nicholas L

et al.

Publication Date

2024-03-01

DOI

10.1029/2023pa004672

The Role of Southeast Asian Island Topography on Indo-Pacific Climate and Silicate Weathering

John. C. H. Chiang[1*], Pierre Maffre[1], Nicholas L. Swanson-Hysell[2], and Francis A. Macdonald[3]

[1]Department of Geography, University of California, Berkeley CA, USA. [2]Department of Earth and Planetary Science, University of California, Berkeley CA, USA. [3]Department of Earth Science, University of California, Santa Barbara CA, USA

* Corresponding author: John Chiang (jch_chiang@berkeley.edu)

547 McCone Hall, University of California, Berkeley CA 94720-4740

Key Points:

- Southeast Asian Island (SEAI) topography enhances local rainfall and moderately increases Indo-Pacific zonal overturning circulation
- SEAI topography significantly increases global silicate weathering and reduces equilibrium atmospheric pCO_2 by ~109 ppm
- Results suggest a significant role for progressive emergence of SEAI topography to cause global cooling over the last several million years

Abstract

The geography of the Southeast Asian Islands (SEAI) has changed over the last fifteen million years, as a result of tectonic processes contributing to both increased land area and high topography. The presence of the additional land area has been postulated to enhance convective rainfall, facilitating both increased silicate weathering and the development of the modern-day Walker circulation. Using an Earth System Model in conjunction with a climate-silicate weathering model, we argue instead for a significant role of SEAI *topography* for both effects. SEAI topography increases orographic rainfall over land, through intercepting moist Asian-Australian monsoon winds and enhancing land-sea breezes. Large-scale atmospheric uplift over the SEAI region increases by ~14% as a consequence of increased rainfall over the SEAI and enhancement through dynamical ocean-atmosphere feedback. The atmospheric zonal overturning circulation over the Indo-Pacific increases modestly arising from dynamical ocean-atmosphere feedback, more strongly over the tropical Indian Ocean. On the other hand, the effect of the SEAI topography on global silicate weathering is substantial, resulting in a ~109 ppm reduction in equilibrium pCO_2 and decrease in global mean temperature by ~1.7 ºC. The chemical weathering increase comes from both enhanced physical erosion rates and increased rainfall due to the presence of SEAI topography. The lowering of pCO_2 by SEAI topography also enhances the Indo-Pacific atmospheric zonal overturning circulation. Our results support a significant role for the progressive emergence of SEAI topography in global cooling over the last several million years.

1. Introduction

The areal extent and topography of the Southeast Asian Islands (SEAI) increased over the past 15 million years (Ma) due to arc magmatism and collisions between the Australian-Indian and Eurasian plates and intervening arc terranes (Hall, 2017; Park et al., 2020). Tectonic uplift through arc-continent collision has been particularly pronounced in New Guinea where a spine of high peaks in the Central Range exceeds 4500 m of elevation within 5º of the equator (Martin et al. 2023). New Guinea grew upward and then outward. A consistent pattern of exhumation from 10 Ma to the present day is recorded by geological and thermochronological data from multiple locations in New Guinea's Central Range (Weiland & Cloos, 1996; Crowhurst et al., 1996; Hill et al., 1989, Martin et al. 2023). After high topography formed in the Central Range, a more recent pulse of uplift occurred in the past 3.7 Ma in the Coastal Range on the northern margin of New Guinea (Abbott et al., 1994), resulting in the Pleistocene emergence of broad floodplains and a secondary topographic high with peaks that exceed 2000 m (Aiello et al., 2019). These topographic barriers also grew progressively in length with Pliocene-Pleistocene uplift of NW New Guinea (Webb et al, 2019), Timor (Tate et al., 2015), Sulawesi (Hennig et al., 2017), and Borneo (Cottam et al., 2013). Today, high topography extends >6,000 km along strike with mountainous tropical islands from western Sumatra to eastern New Guinea (a significantly wider region than the ~4,500 km width of the continental United States; Hall, 2017).

The presence of these islands–called the 'Maritime Continent' by meteorologists (Ramage 1968)–is presumed to control the rainfall climate of that region. The SEAI have been framed as the 'tropical heat engine' due to their role in global poleward heat transport (Ramage 1968). Satellite observations show that more rainfall occurs over the islands than over the neighboring oceans (Sobel et al. 2011, Biasutti et al. 2012), leading to the hypothesis that the presence of the islands increases the overall convection over the SEAI through driving diurnal land-sea breezes and convection (Sato et al. 2009, Liberti et al. 2001, Cronin et al. 2015). In this view, the increase in the land surface area, surrounded by a warm ocean, is key to the increase in SEAI rainfall (Dayem et al. 2007).

The emergence of the SEAI during the Miocene and Pliocene has been postulated to be a control on Earth's climate over million-year timescales. Dayem et al. (2007) argued from empirical grounds that the increase in the SEAI rainfall leads to an enhancement of the Walker circulation (i.e. the Pacific portion of the zonal overturning circulation), and hence the east-west asymmetry in sea surface temperature (SST) of the tropical Pacific through the Bjerknes feedback. Following this idea, Molnar and Cronin (2015, hereafter MC15) argued that the emergence of the SEAI facilitated the creation of the modern east-west gradient in tropical Pacific SST thereby ending the 'permanent El Niño-like' conditions of the Pliocene. In this scenario, northern North America cooled as a consequence of atmospheric teleconnections from the tropical Pacific altering the trajectory of the jet stream, similar to what occurs during La Niña events today (Molnar and Cane 2002, Huybers and Molnar 2007, Vizcaino et al. 2010).

MC15 also argued that increased silicate weathering over the SEAI lowered atmospheric CO_2 concentrations, but this effect was small in their model compared to later analyses (c.f. Park et al., 2020, Martin et al., 2023) as it implements a lower percentage of global chemical weathering in the SEAI (see section 6.3 for a discussion on this point). It is estimated that the SEAI currently accounts for ~11.5% of the global weathering rate, of which New Guinea contributes 44% of the SEAI weathering rate (Martin et al., 2023). The SEAI are a major CO_2 sink in part because they contain abundant igneous rocks including Mg- and Ca-rich mafic and ultramafic lithologies (Macdonald et al., 2019), unlike localities such as Taiwan, which is dominated by catchments formed of sedimentary rocks that can either be net sources or sinks of carbon (e.g. Hilton and West, 2020, but c.f. Maffre et al., 2021). According to MC15, these two mechanisms, enhanced Walker circulation and increased global weatherability, caused the onset of Northern Hemisphere glaciations starting ~3 million years ago.

These arguments point, directly or implicitly, to the role of increased SEAI land surface area in increasing SEAI rainfall. However, literature on modern-day SEAI rainfall and its interannual variability point instead to the role of SEAI topography on rainfall through intercepting moist monsoonal flow (Chang et al. 2005, Robertson et al. 2015). The SEAI is embedded in a strong cross-equatorial monsoon flow between the continents of Asia and Australia that reverses with the seasons (Figure S1). High SEAI topography, especially over New Guinea, intercepts this monsoonal flow and the resulting orographic uplift induces precipitation. Chang et al. (2005) describe this effect succinctly: "*The annual cycle [of rainfall] is dominated largely by interactions between the complex terrain and a simple annual reversal of the surface monsoonal winds throughout all monsoon regions from the Indian Ocean to the South China Sea and the equatorial western Pacific.*"

High-resolution rainfall data corroborates this view by showing rainfall over New Guinea following the high topography and rain shadows downstream (Biasutti et al. 2012). Sobel et al. (2011) noted the orographic enhancement of rainfall over tropical islands in high-resolution satellite rainfall data, and pointed to the lack of a clear diurnal signal in this enhancement as evidence for mechanically-forced upslope flow. More generally, Xie et al. (2006) highlighted the role of narrow mountains in setting the large-scale organization of Asian Monsoon convection, in regions such as the Western Ghats, the Southern Indo-Burman Range, and Annamese Range, underscoring their orographic origins. A theoretical basis for tropical orographic precipitation was formulated by Nicolas and Boos (2022), showing that such rainfall could result from the effect of orographic stationary gravity waves on the lower-tropospheric convective quasi-equilibrium state. In an atmospheric general circulation model study with imposed sea surface temperature, Zhang et al. (2019) showed that SEAI topography increases local rainfall due to its dynamical lifting effect. Topography has also been argued to enhance diurnal tropical island rainfall through elevated land heating and through associated convective feedback (Zhou and Wang 2006), distinct from the mechanical effects of topography on rainfall.

We hypothesize that the emergence of SEAI *topography* was central to the formation of the SEAI rainfall climate, and thus to both the enhancement of the tropical Pacific east-west SST gradient as well as enhanced silicate weathering and associated CO_2 drawdown. We argue that the rapid uplift of SEAI topography during the late Miocene and Pliocene significantly increased rainfall, enhanced physical erosion rates and elevated silicate weathering fluxes. To test this hypothesis, we explore the role of SEAI topography, using simulations of an Earth system model varying SEAI topography to explore how rainfall over the SEAI changes, and also its effect on the tropical ocean-atmosphere system. We also explore the consequences of increased topography on global silicate weathering and CO_2 using a coupled climate-silicate weathering model.

2. Materials and Methods

2.1 Earth System Model

We use the Community Earth System Model version 1.2 (CESM1.2; Hurrell et al. 2013), which has been used in a number of studies examining the rainfall climate of the Maritime Continent (e.g. Zhang et al. 2019, Chen et al. 2021, Ren et al. 2023). For the atmosphere and land components, we choose the CAM5 atmosphere and CLM4.0 land model with satellite phenology and using a standard finite volume 0.9° x 1.25° grid. For the ocean, we use two configurations. The primary configuration we use is a global slab ocean model at the same grid resolution as the atmosphere. The slab ocean approximates a well-mixed ocean surface layer at every gridpoint, and with climatological monthly ocean heat flux convergence (aka 'q-flux') values imposed that substitute for the effect of a dynamical ocean; we use a standard q-flux boundary condition provided with CESM1.2 derived from a fully-coupled preindustrial simulation. The reason for using a simplified ocean is to allow for a relatively short equilibration time for the climate system under climate forcings in particular pCO_2 scenarios. This approach enables more efficient estimates of pCO_2 change following changes to weathering fluxes (see section 2.2). A prognostic sea-ice component is also used. This combination of atmosphere, land, ocean, and sea-ice components under a preindustrial configuration (in particular with pCO_2 set to 284.7 ppm) is identified in the CESM1.2 code as the E_1850_CAM5 component set. In the text, we refer to this configuration as the *slab ocean model.* The slab ocean simulations are run for 70 years each with the last 30 years used for climatology. We evaluate the climate uncertainty treating each year in the 30-year interval as an independent sample; in particular, we evaluate the 95% confidence interval as ± 1.96 times the standard error of the 30-yr sampled climate data.

The second ocean configuration we use is the fully dynamical Parallel Ocean Program version 2 ocean model using a ~1° grid with the pole displaced to Greenland (referenced as gx1v6 in the CESM 1.2 code); a prognostic sea-ice component is also used. This configuration is used to assess the dynamical ocean-atmosphere adjustments associated with changing SEAI topography, following the claims made by MC15 for the Walker circulation. This combination of atmosphere, land, ocean, and sea-ice components under a preindustrial configuration is identified in the CESM1.2 code as the B_1850_CAM5 component set. In the text, we refer to this configuration as the *fully coupled model.* The fully coupled simulations are run for 110 years each, with the last 70 years used to form the climatology. The tropical ocean-atmosphere adjustment timescales are relatively short, but a longer sampling period is needed to estimate the mean changes (as compared to the slab ocean simulations) because the dynamical ocean-atmosphere coupling induces larger interannual climate fluctuations in the tropics especially from the El Niño-Southern Oscillation (ENSO). Due to limited computational resources, the fully-coupled simulations are not sufficiently long to allow for deep-ocean adjustments, and this fact should be considered as a limitation to our simulations. The amplitude of ENSO in the CESM1.2 is slightly larger than observed, and the spatial pattern of the SST warming during the ENSO warm phase extends too far to the west (Zhang et al. 2017).

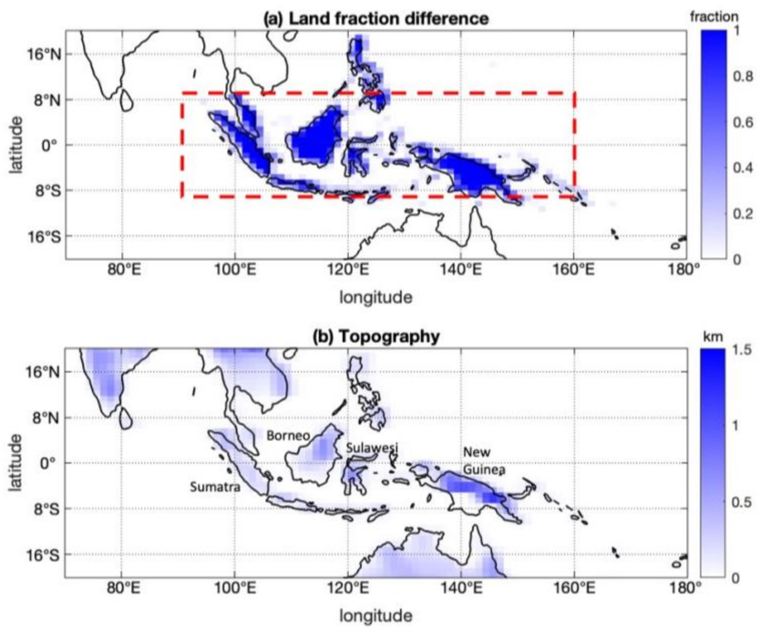

Figure 1. Geographical configuration of the simulations. (a) Land grid points identified as part of the Southeast Asian Islands (SEAI), shown as the change in the land fraction from the no SEAI case to the modern SEAI case. The ***SEAI region*** is defined by the box encompassed by the dashed red lines, 9°S-9°N and 90°-160°E. ***SEAI region land*** is the subset of the SEAI region with the land fraction > 0.1 in the modern SEAI simulation; the opposite is assigned as ***SEAI region ocean***. (b) Standard modern-day topography in the CESM1.2 at the resolution of the model. Names of the major islands in the SEAI are labeled.

Our primary set of simulations involve modifying the topography of the SEAI to assess their climate effects; we apply this change both for the slab ocean and fully coupled configurations. The grid points for land surface modification are as shown in Figure 1a. Over these points, the height of the model topography (Figure 1b) is modified by multiplying the default value by a fraction, from 0 to 1.5 in steps of 0.5. This topographic change also affects the gravity wave parameterization through altering the surface roughness. All other land surface properties are kept the same, including the plant functional type. We call these simulations '0% SEAI topography' (aka flat SEAI), '50% SEAI topography', '100% SEAI topography' (aka modern SEAI), and '150% SEAI topography' simulations, respectively (see Table 1 for a list of simulations).

In the slab ocean simulation, we additionally replace the SEAI (gridpoints colored blue in Figure 1a) with a slab ocean of 16 m depth, chosen to approximate the depth of the ocean immediately surrounding the islands. In this instance, the SEAI is represented by a slab ocean along with the rest of the model ocean. We apply this change to assess the climate change from the introduction of the SEAI land surface. We assume no ocean heat flux convergence over these grid points. We call this the 'no SEAI' simulation (see Table 1). These two choices – depth and ocean heat flux convergence – may significantly determine the climate response to the removed land. For this reason, the results from this simulation should not be interpreted as the definitive response to a 'no land' situation, as the type of ocean that replaces the land matters (see section 6.3 for a discussion on this). To test the sensitivity of our no SEAI simulation, we undertake two additional simulations, one on which the mixed layer depth of the imposed slab ocean is doubled to 32 m, and another on which we impose a constant 20 W/m^2 ocean heat flux convergence (20 W/m^2 being the typical annual average ocean heat flux convergence in the oceans surrounding the SEAI).

Our simulations are similar to Zhang et al. (2019) who also investigated the role of the SEAI land surface and terrain on the climate of the Maritime Continent. They also used the CESM1.2, but with prescribed sea surface temperature and sea-ice cover (1979-2005) from observations, and undertook simulations flattening topography and replacing SEAI with ocean. With the latter, they replaced the SEAI with prescribed SST interpolated from the surrounding ocean. Our simulations differ methodologically in using an interactive ocean, which is necessary for our purposes of evaluating the global mean temperature changes (using the slab ocean) and the zonal overturning circulation (fully coupled ocean). While Zhang et al. (2019) also investigated the climate effects of the SEAI, the purpose of the two studies are different. Zhang et al. (2019) focused on the climate dynamics of the Maritime Continent rainfall climate and seasonal evolution, whereas our study is motivated from geological history following MC15 and Martin et al. 2023, addressing silicate weathering and impact on tropical ocean-atmosphere interactions and zonal overturning circulation.

To aid our quantification of the climate changes over the SEAI, we define the *SEAI region* to be the area bounded by the red dashed lines in Figure 1a (9ºS-9ºN, 90ºE-160ºE), which covers most of the SEAI with high topography. *SEAI region land* is the subset of the SEAI region with the land fraction > 0.1; the opposite is assigned as *SEAI region ocean*.

Figure S1 shows the comparison of the simulated rainfall and lower tropospheric wind seasonal climatology between the slab ocean simulation with rainfall from the Tropical Rainfall Measuring Mission (TRMM; Huffman et al. 2007) and 850mb winds from the European Centre for Medium-Range Weather Forecasts Reanalysis version 5 (ERA5; Hersbach et al. 2020) with the resolution regridded to match the CESM1.2. The fully-coupled simulation quantitatively resembles that for the slab ocean. The control run is preindustrial whereas the TRMM and ERA5 are for modern-day, but this is not an issue for our purpose which is a qualitative comparison of the seasonal climatology. The annual mean field (Figure S1, top panels) shows that the northeasterly and southeasterly trade winds are captured in the CESM1.2, and that there are peaks in rainfall over Borneo and also over New Guinea concentrated on the Central Range of high topography. Rainfall over Sumatra is less well-captured, showing a dry bias in the model relative to TRMM observations. Our results are similar to those of Zhang et al. (2019) who find that the seasonal cycle of rainfall has a dry bias over the western Maritime Continent where it is relatively flatter, and a wet bias over the eastern Maritime Continent where it is more mountainous.

The CESM1.2 simulates the seasonal change in the magnitude of the northeasterly and southeasterly trades between the winter and summer months. Gross seasonal changes in rainfall are also captured, including the December-February and March-May peak in New Guinea rainfall. A notable discrepancy is the simulated rainfall over Borneo during December-February where it is significantly underestimated. Examination of a published 0.25°x0.25° resolution simulation of the CESM1.3 (Chang et al. 2020) shows that while the dry Borneo rainfall bias is improved with increased atmospheric resolution, the wet bias over New Guinea is not (Figure S2). While this resolution is better able to resolve the topography, there is an intense wet bias over New Guinea where rainfall straddles the Central Range (Figure S2a). This is unlike in observations, where annual mean rainfall falls on either side of the range (Figure S2b).

In summary, the CESM1.2 captures the mean trades and seasonality of the low-level tropospheric flow over the region, and the seasonality of the rainfall over the SEAI. The main difference with observations is an annual mean dry bias over the Sumatra and Borneo – islands with lower topography – and a wet bias over New Guinea, an island with higher topography. This suggests that the simulated rainfall may be too sensitive to the topographic influence, with implications for the estimates of silicate weathering fluxes (see section 6.3 for a discussion).

2.2 Climate-Silicate Weathering Model

We use the spatially resolved silicate weathering model GEOCLIM to estimate the combined effects of changes in slope, temperature, and runoff on silicate weathering and to develop estimates of the effect on long-term steady-state CO_2 levels. The model focuses on the weathering of Ca- and Mg-bearing silicate minerals whose weathering leads to CO_2 sequestration on geologic timescales. We use the version of the model as formulated and calibrated in Park et al. (2020) which is based on the parameterizations of chemical weathering rate as a function of temperature and runoff as derived by Gabet and Mudd (2009) and West (2012) (see Text S1 for details). The global lithological map used is GLiM (Hartmann and Moosdorf, 2012); we omit regions of carbonate lithology from the analysis and only compute the weathering of silicate lithologies. The calibration of the model parameters, conducted by Park et al. (2020), is based on comparison of modeled chemical weathering fluxes to data from 80 modern watersheds. Park et al. (2020) selected 573 model parameterizations (i.e., unique parameter combinations) that yield data-model r^2 from 0.5 to 0.57. The model is sensitive to physical erosion rates, as the weathering front propagates downward at the rate of surface erosion, which controls the flux of primary minerals undergoing chemical weathering and the time that minerals spend in the chemically weathering profiles. The two competing effects determine how erosion rates influence the efficiency of weathering reactions. The physical erosion rate in GEOCLIM is parameterized to be proportional to slope and to the square root of runoff. For climate inputs, we provide the weathering model with climatological annual mean land runoff and surface temperature as simulated by the CESM1.2 in slab ocean mode. For each case considered, an ensemble of 573 simulations with identical boundary conditions is performed, only changing the model's parameters. We use the 573 selected unique parameter combinations from Park et al. (2020) that best fit the modern watershed data. When reporting GEOCLIM output we use the mean of the 573 parameter combinations as our best estimate and account for climate uncertainty associated with this mean.

The global long-term CO_2 consumption rate from the calibrated model, estimated by running the weathering model with pre-industrial boundary conditions, overlaps with estimates of non-anthropogenic global CO_2 emission which is expected for a system near steady-state. In practice, the "control" simulation assigns a specific CO_2 degassing rate to each of the 573 parameter combinations with the assumption that CO_2 consumption by weathering must balance

CO_2 degassing (Siever, 1968; Walker et al., 1981; Berner and Caldeira, 1997). When running the model with modified SEAI boundary conditions, we compute, for each parameter combination, the atmospheric pCO_2 level at which global silicate weathering rate balances the corresponding CO_2 degassing by interpolating between climate runs with different pCO_2. To this end, we undertook additional CESM1.2 slab ocean simulations where we double pCO_2 to 569.4 ppm for each of the simulation cases where this is needed (no SEAI and flat SEAI). For a specified pCO_2 level between preindustrial and double pCO_2, the corresponding annual mean surface temperature and land runoff spatial fields is derived by assuming a log(pCO_2) linear interpolation between these two simulations. These interpolated fields are then applied to GEOCLIM to estimate a corresponding global weathering rate. The pCO_2 level such that the global weathering rate equals the original volcanic degassing. This interpolation method has been widely used in the GEOCLIM model framework: Donnadieu et al. (2004), Le Hir et al. (2011), Godderis et al., (2017) used a pCO_2 linear interpolation, whereas Park et al., (2020), Maffre et al. (2021), Marcilly et al. (2022), and Maffre et al. (2023) used a log(pCO_2) linear interpolation.

We also apply GEOCLIM to the flat SEAI (0% SEAI topography) simulation in order to quantify the weathering contribution from land area in the absence of topography. Since the physical erosion rate in GEOCLIM is parameterized to be proportional to slope and to the square root of runoff (Park et al. 2020), we modify the topography in GEOCLIM accordingly. We do not use a zero slope field, which would result in zero erosion and zero weathering, but instead use a uniform slope of 1.23%, that is, the average slope of global land surface below 200 m (Maffre et al., 2018).

3. Rainfall Changes with SEAI

We first examine the slab ocean simulations for changes to rainfall resulting from changes to the SEAI. Starting from a no SEAI configuration where the land is replaced with a slab ocean of 16 m depth, the introduction of the SEAI (with the present-day topography) increases rainfall over virtually all of the SEAI (Figure 2a). Rainfall over the surrounding ocean, in particular to the north of New Guinea, is generally reduced. Surface wind changes show convergence into the SEAI region, with anomalous westerlies to the west of the SEAI, and easterlies to the east and north of the SEAI. This flow response is qualitatively consistent to large-scale diabatic heating symmetric about the equator (Gill 1980).

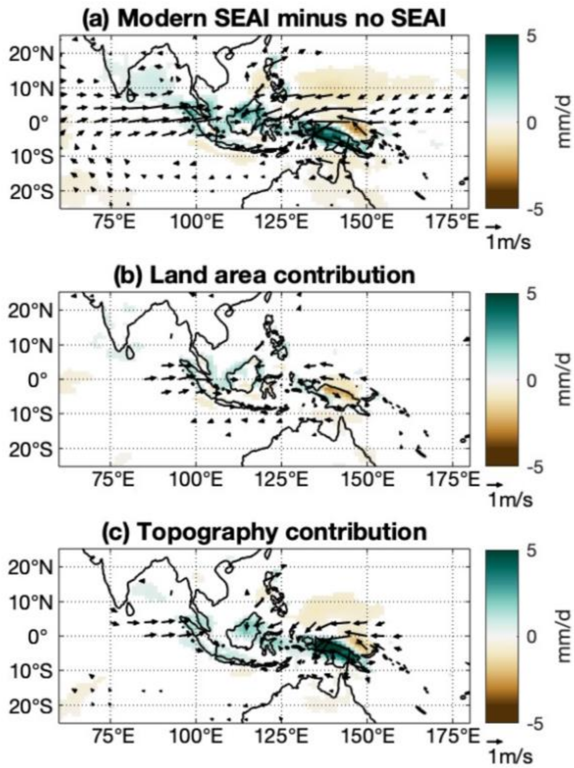

Figure 2. Annual mean change to the rainfall (shaded, in mm/d) and 925 mb winds (reference vector 1 m/s). (a) Modern SEAI minus no SEAI, showing change in rainfall associated with introduction of the SEAI (both land area and topography). **(b)** The land area contribution to (a), calculated as flat SEAI minus no SEAI. **(c)** The topography contribution to (a), calculated as modern SEAI minus flat SEAI. Precipitation changes are plotted only if significant at the 5% level (using a two-sided t-test). Wind vectors are only plotted if either the zonal or meridional wind change is significant at the 5% level (two-sided t-test).

Separating the contributions to land area (Figure 2b) and topography (Figure 2c) shows that most of the contribution to the increase in rainfall comes from the introduction of modern SEAI topography, especially over New Guinea, Sulawesi, and northern Borneo where there is significant relief (Figure 1b). There are seasonal differences in the relative contributions from land and topography. The land surface contributions are strongest during the equinox seasons (Figure 3, left panels), and in fact contribute to a rainfall decrease (as compared to having the slab ocean over the SEAI region) during the solstice seasons; the net effect on annual mean rainfall of each location is small as a result. We found this qualitative behavior of the land area contribution to be insensitive to selected changes in the no SEAI slab ocean properties, namely doubling the mixed layer depth to 32 m and imposing a 20 W/m^2 ocean heat flux convergence (Figure S3). In contrast, the topographic contribution is positive across all seasons, with slight variations to the magnitude. The increase in rainfall associated with topography is especially

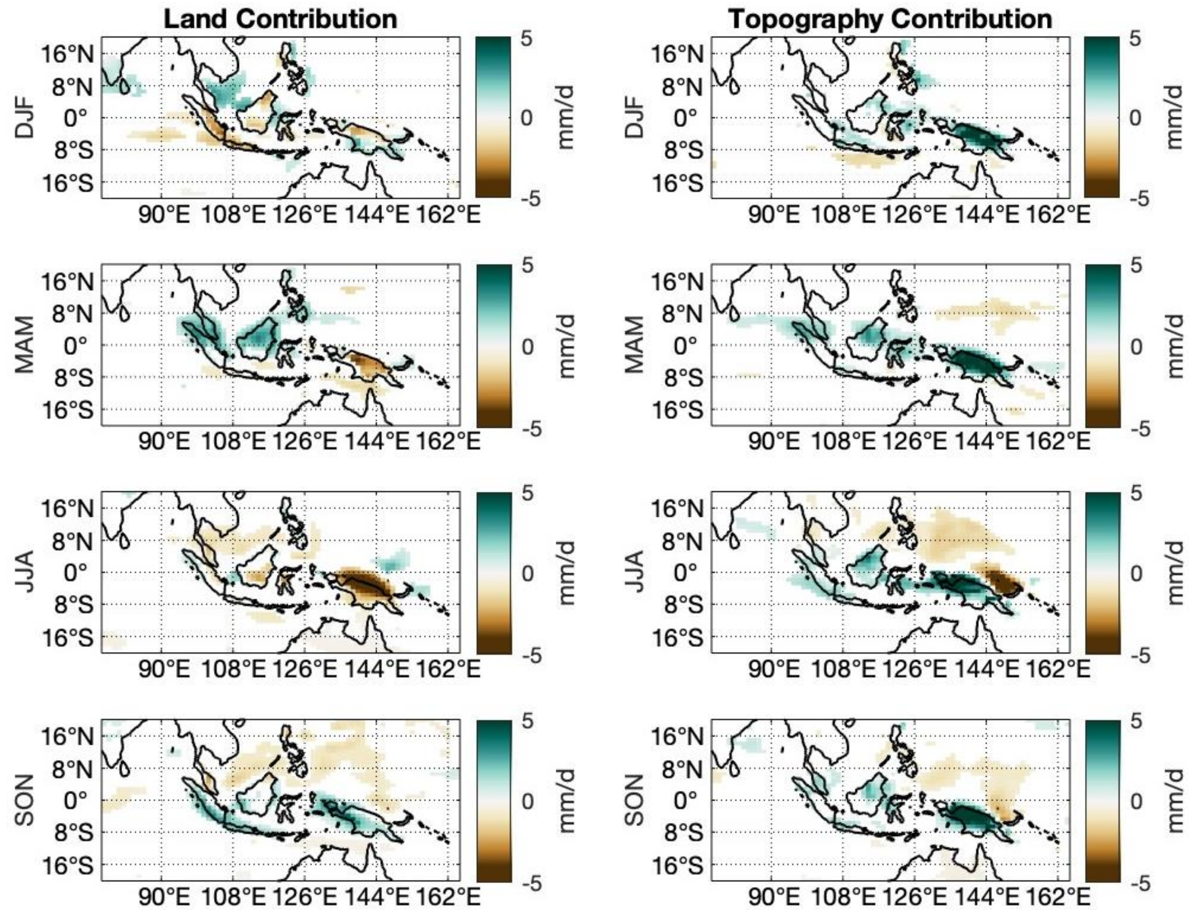

Figure 3. Seasonal land area (left panels) and topography (right panels) contributions to SEAI rainfall, for Dec-Feb (top row), Mar-May (second row), Jun-Aug (third row), and Sep-Nov (bottom row). Land area contributions are strongest during the equinox seasons, but topography contributions are strong year-round. Precipitation changes are plotted only if significant at the 5% level (using a two-sided t-test).

pronounced over New Guinea (Figure 3, right panels). The increase in rainfall across all seasons with SEAI topography is consistent with the findings of Zhang et al. (2019). They used CESM1.2 with fixed sea surface temperature whereas our approach uses a slab ocean, which indicates that thermodynamic ocean-atmosphere feedback does not qualitatively alter the rainfall response to SEAI topography.

We now evaluate the change to rainfall averaged over the land in the SEAI region. Starting with a slab ocean-covered SEAI, the introduction of flat land does not significantly change the average rainfall over SEAI region land (Figure 4a, contrast the green data indicated by the cross to the green data indicated by the filled circle, both near 0% relative elevation). This result is insensitive to selected changes in the no SEAI slab ocean properties imposed over former land grid points, namely doubling the mixed layer depth to 32 m and imposing a 20 W/m^2 ocean heat flux convergence (Figure S4a). However, increases in SEAI topography lead to an increase in average rainfall over SEAI region land (Figure 4a, green line), from 7.0 mm/d at 0% to 8.7 mm/d at 100% SEAI topography (a 24% increase), and to 10.0 mm/d at 150% SEAI topography (42% increase). Over the SEAI region ocean, precipitation remains relatively constant at around 7.7 mm/d regardless of SEAI topography (Figure 4a, blue data). Thus, average rainfall over the SEAI region increases slightly with increasing SEAI topography, due to the increased rainfall over SEAI region land (Figure 4a, black data). These results for topography are generally consistent with those found by Zhang et al. (2019).

Over SEAI region land, higher terrain gets the larger share of the rainfall increase as SEAI topography is increased. Figure 4b shows the increase in average rainfall masked over the modern SEAI topography at various elevations. These elevation masks are the regions

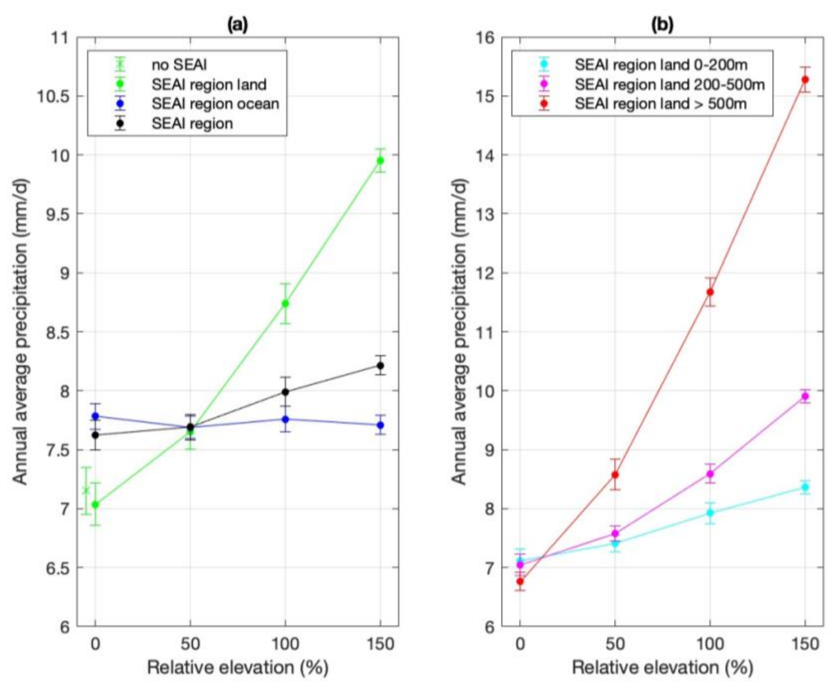

Figure 4. Change to SEAI rainfall with SEAI topography. (a) Annual average precipitation as a function of SEAI topography from 0% to 150% for SEAI region land (green dots), SEAI region ocean (blue dots), and SEAI region (black dots). Average precipitation over the SEAI region land for the no SEAI case is also shown by the green cross. **(b)** Annual average rainfall over SEAI region land masked in terms of modern-day elevation. Cyan dots: elevations between 0-200m; magenta dots: elevations between 200-500m; and red dots: elevations > 500m. Note that the y-axis scale differs from (a). Error bars indicate the 95% confidence interval of the mean, calculated as +-1.96 times the standard error of the sampled data.

corresponding to the modern elevation from 0-200 m (cyan dots), 200-500 m (magenta dots), and >500 m (red dots). For the area of SEAI region land with modern elevation greater than > 500 m, average rainfall goes from 6.8 mm/d at 0% SEAI topography to 11.7 mm/d at 100% SEAI topography, a 73% increase. This increase is much larger than the 11% increase over the same interval for the 0-200 m SEAI region land, and 22% for the 200-500 m SEAI region land.

4. Zonal overturning circulation response

Dayem et al. (2007) and MC15 postulated that the increase in SEAI rainfall would increase the Walker circulation, based on observations showing a positive correlation between the two. They also argue that the positive Bjerknes feedback (Bjerknes 1969) would leverage the increase in the Walker circulation to enhance the east-west temperature gradient in the equatorial Pacific. Our simulations showing the increase in SEAI rainfall with topography provides a scenario to explore this hypothesis.

We first examine the tropical large-scale circulation response to SEAI topography in the slab ocean simulations without the dynamical ocean-atmosphere interaction (Figure 5a-d). The introduction of the modern SEAI (from a no SEAI situation) increases atmospheric uplift over the SEAI region by ~4.7 mb/day (a ~14% increase). Topography provides the larger contribution, contributing ~67% of that response (Figure S5a, black data points). This result is insensitive to selected changes in the no SEAI slab ocean properties, namely doubling the mixed layer depth to 32 m and imposing a 20 W/m^2 ocean heat flux convergence (Figure S4b). The topographic influence of the modern SEAI (compared to flat SEAI) contributes to warmer SST surrounding the SEAI by a few tenths of a degree (Figure 5a), and anomalous zonal winds converging to the SEAI with anomalous westerlies over the equatorial Indian Ocean and anomalous easterlies over the western equatorial Pacific (Figure 5a), suggesting an increase in the large-scale uplift over the SEAI. Indeed, large-scale atmospheric uplift increases over the SEAI region land is focused over regions with topography (as indicated by the negative pressure velocity anomalies in Figures 5b and 6a), and increases with increasing topography (Figure S5a, green line). Averaged over the SEAI region, however, the increase in atmospheric uplift is modest: the modern SEAI topography contributes only about 8.8% to the mean atmospheric uplift over the SEAI region (Figure S5a black line, and Figure 7).

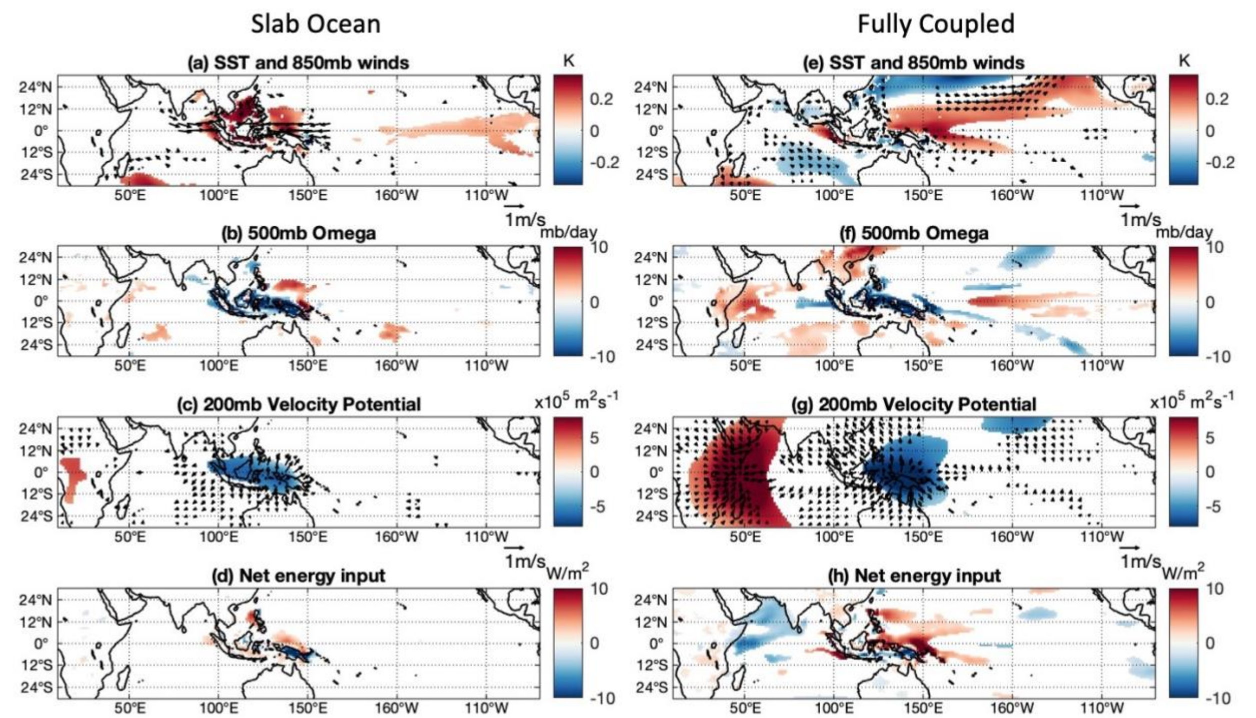

Figure 5. SEAI topography contribution to the large-scale response (modern SEAI minus flat SEAI). Left panels (a-d) are for slab ocean simulations, and right panels (e-h) are fully-coupled simulations. **(a and e)** SST (K) and 850 mb winds (reference vector 1 m/s). **(b and f)** 500 mb pressure vertical velocity (mb/day). **(c and g)** 200 mb velocity potential (x10^5 m^2s^{-1}) and divergent component of horizontal winds (reference vector 1 m/s) **(d and h)** Net energy input into the atmosphere (Wm^{-2}). Scalar field changes are plotted only if significant at the 5% level (using a two-sided t-test). Vectors are only plotted if either the zonal or meridional wind change is significant at the 5% level (two-sided t-test). The upper-tropospheric velocity potential is a commonly-used diagnostic of the atmospheric zonal overturning circulation (e.g. Kumar et al. 1999), with positive values indicating anomalous subsidence and negative values indicating anomalous uplift; the negative of the gradient of the velocity potential gives the divergent component of the horizonal winds. The net energy input (NEI) is the total vertical energy flux into the atmospheric column, with contributions from radiation at both top-of-atmosphere and surface, and latent and sensible fluxes from the surface. In the tropics, a positive NEI is typically balanced by an increased atmospheric uplift and upper-tropospheric divergence that acts to export energy horizontally (Zeng and Neelin 1999, Biasutti et al. 2018); NEI thus provides a diagnostic connection between uplift/subsidence with top-of-atmosphere and surface energy flux changes.

Where does the uplifted air go? The horizontal divergent flow at 200 mb shows mass divergence over the SEAI (Figure 5c). Compensating subsidence appears largely focused over the western North Pacific to the north, northeast and east of the SEAI (Figures 5b,c and 6a). Notably, there is no significant subsidence response over the central and eastern equatorial Pacific. The lack of a zonal overturning circulation response in the Pacific is consistent with the weak (~0.1K) SST warming over the eastern equatorial Pacific, which reduces the zonal east-west SST contrast across this region (Figure 5a). Since the model configuration is a slab ocean,

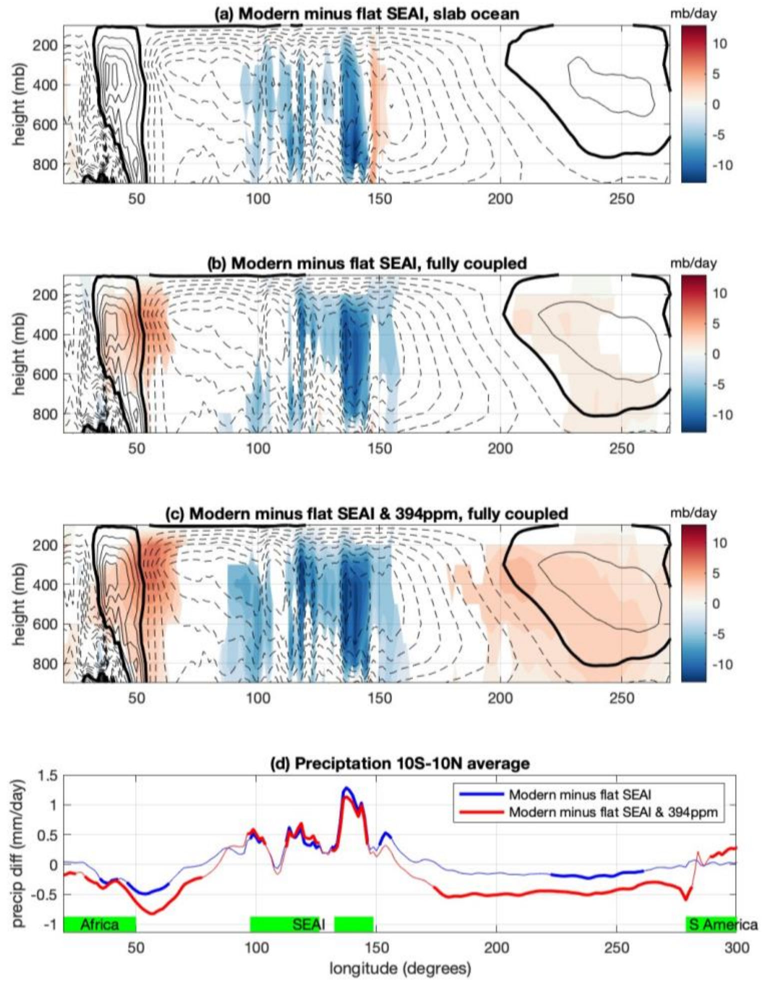

Figure 6. SEAI topographic contribution to the zonal overturning circulation and precipitation over the Indo-Pacific. (a) Annual mean pressure vertical velocity averaged over 10°S-10°N. Contours show its climatology for the slab ocean modern SEAI simulation, and the shaded area is the difference between the modern SEAI and flat SEAI indicating the contribution by the SEAI topography. The contour interval is 5mb/day, and the zero contour is in bold. Vertical velocity changes are plotted only if significant at the 5% level (using a two-sided t-test). **(b)** Same as (a), but for the fully coupled simulations. **(c)** Same as (a), but for the difference between the modern SEAI and flat SEAI & 394ppm, indicating the contribution by SEAI topography and reduction in $p\text{CO}_2$. **(d)** Annual mean precipitation difference (averaged over 10S-10N) for the fully-coupled simulation, modern SEAI minus flat SEAI (in blue) and modern SEAI minus flat SEAI & 394ppm (in red). Thicker lines indicate that the change is significant at the 5% level (using a two-sided t-test). Locations of land areas are indicated in green.

the warming has to originate from changes to surface fluxes. However, there is also a noticeable increase in the equatorial surface easterlies over the western Pacific resulting from modern SEAI topography with a ~5% strengthening of the mean easterlies over the western equatorial Pacific relative to flat SEAI (Figure 5a). This strengthening of the easterlies could trigger an enhancement of the Walker circulation through dynamical ocean-atmosphere feedback, as argued by MC15. Anomalous westerlies also occur to west of the SEAI that could induce a dynamical ocean-atmosphere response over the tropical Indian Ocean.

Motivated by the observation of anomalous zonal winds over the equatorial Indian and Pacific Oceans, we examine the additional effect of modern SEAI topography from the dynamical ocean-atmosphere feedback by contrasting the change resulting from the fully-coupled simulations with that of the slab ocean simulation ('enhanced' or 'reduced' in this paragraph is in reference to this comparison). Dynamical ocean-atmosphere feedback increases the upper-tropospheric mass divergence over the SEAI (Figure 5g) and enhances the atmospheric uplift over the SEAI region such that topography now contributes 13.5% to the mean uplift (Figure 7); it is however still modest. Moreover, a change to the zonal overturning circulation now appears over both the tropical Indian and Pacific Ocean basins. The tropical Indian Ocean zonal overturning circulation is enhanced with increased subsidence (Figures 5f,g and 6b) and reduced rainfall (Figure 6d, blue line) over the western equatorial Indian Ocean. For the tropical Pacific, there is a small enhancement of the east-west equatorial SST contrast mainly because of a warmer western Pacific SST, with the eastern equatorial Pacific SST essentially unchanged (Figure 5e). A weak increase in subsidence occurs over the eastern equatorial Pacific (Figure 6b) as well as a small but significant decrease in precipitation (Figure 6d, blue line). Thus, dynamical ocean-atmosphere interactions in the Pacific act to negate the weak warming in the eastern equatorial Pacific in the slab ocean simulation, and modestly enhance the Walker circulation.

The thermocline responses over the equatorial Indian and Pacific Oceans indicate that the anomalous equatorial zonal wind changes to SEAI topography seen in the slab ocean (Figure 5a) elicit an ocean dynamical response (Figure 8). The thermocline shallows in the western equatorial Indian Ocean (indicated by cooling around 100m depth in Figure 8b) consistent with the anomalous westerlies over the eastern equatorial Indian Ocean. In the equatorial Pacific, the thermocline deepens in the west and shallows in the east (Figure 8b), steepening the climatological west-to-east tilt of the equatorial thermocline (Figure 8a). These thermocline changes are consistent with driving the equatorial SST gradient changes in the Indian and Pacific Oceans that enhance the zonal overturning circulation in both basins, though it should be stated that the changes are modest.

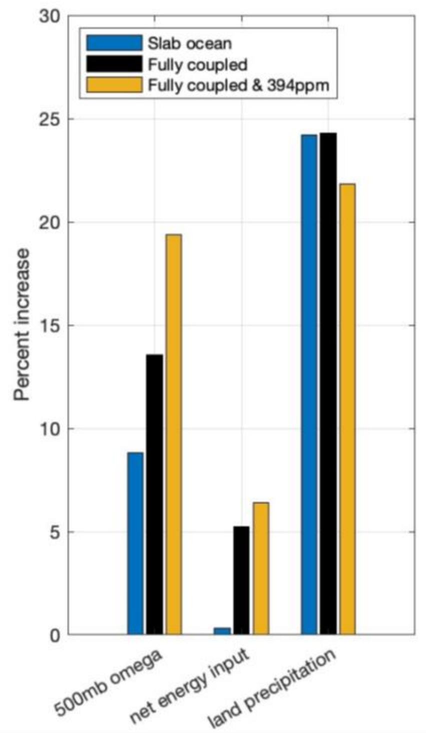

Figure 7. Comparing the topography contribution between slab ocean and fully coupled simulations. Percentage increase of annually averaged climate variables between the modern SEAI and flat SEAI. Percentage increase is relative to the value for flat SEAI. From left to right: 500mb vertical velocity averaged over the SEAI region; net energy input into the atmosphere averaged over the SEAI region; and precipitation averaged over SEAI region land. Blue bars are for the slab ocean simulation, black bars for fully coupled simulation, and orange bars are for fully coupled simulation using flat SEAI & 394ppm CO_2 as the baseline.

The net energy input into the atmosphere (NEI) – i.e. the sum of the top-of-atmosphere and surface energy flux into the atmospheric column – gives another indication of how this zonal overturning response comes about (Figure 5d,h). Assuming fixed gross moist stability and negligible horizontal moist static energy convergence, an increase in the NEI results in stronger uplift and upper-level divergence that acts to export the energy horizontally (Zeng and Neelin 1999). In the slab ocean simulations, the NEI change arises mainly through the top-of-atmosphere fluxes as the surface has relatively small thermal inertia and is thus close to energy balance. While the oceans surrounding the SEAI contribute positively to NEI (i.e., there is energy going into the atmosphere), the NEI directly over the SEAI region land is negative because the shortwave reflection by clouds outweighs its longwave trapping (Figure 5d). The net NEI change over the SEAI region with SEAI topography is thus very weakly positive (+0.33%, Figure 7). There is no significant change to the NEI outside of the SEAI region, consistent with the lack of tropospheric vertical velocity changes. With a dynamical ocean operating, the top-of-atmosphere flux changes remain similar to the slab ocean response, but large surface flux increases occur over the SEAI ocean primarily close to the coastlines of the SEAI that act to increase the NEI over the SEAI region by 5.2% (Figure 5h, Figure 7). On the other hand, NEI is reduced over the western Indian Ocean and over most of the equatorial Pacific east of 155ºE with a concentration around the 180ºE date line, though for the latter only the decrease over the central equatorial Pacific is statistically significant (Figure

5h). Thus, tropical ocean-atmosphere dynamics enhance the zonal overturning circulation over the Indo-Pacific to modern SEAI topography through changes to the ocean heat flux convergence, with the increase most noticeable over the tropical Indian Ocean.

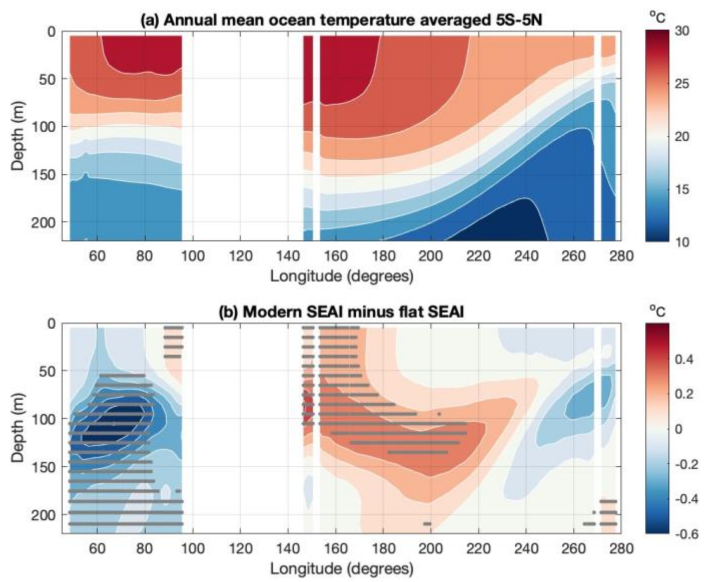

Figure 8. Ocean subsurface response to the introduction of SEAI topography. (a) Annual mean ocean temperature averaged between 5°S-5°N for the fully-coupled modern SEAI simulation, showing the location of the thermocline (approximately following the 20°C isotherm). **(b)** Change in the subsurface temperature between the modern SEAI and flat SEAI simulations (former minus latter). Differences that are significant at the 95% level are indicated by the grey dots. Introduction of SEAI topography shallows the thermocline in the western Indian ocean and eastern equatorial Pacific, and deepens the thermocline in the western Pacific.

Finally, while dynamical ocean-atmosphere feedbacks enhance the atmospheric uplift over the SEAI region and enhanced uplift in turn implies increased convective rainfall, it surprisingly does not enhance rainfall over SEAI land relative to the slab ocean configuration. While modern SEAI topography increases rainfall over SEAI land by 24.2% (relative to 0% topography) in the slab ocean configuration, the corresponding increase for the fully coupled model is 24.3%, essentially the same (Figure 7). The rainfall increase over the SEAI region must therefore occur over the ocean. This difference in the rainfall between SEAI land and SEAI ocean is consistent with the change in NEI: in the fully coupled case compared to the slab ocean case, the NEI over SEAI land is relatively unchanged whereas NEI over the SEAI ocean is altered because of the addition of ocean heat flux convergence.

5. Response of silicate weathering and equilibrium *p*CO_2

We now examine the role of SEAI topography in silicate weathering and the associated effects on the carbon cycle. To this end, we apply the annual mean temperature and runoff from the slab ocean simulations to the GEOCLIM model to assess changes to silicate weathering. We also estimate the *p*CO_2 and resulting global mean temperature change that would result in a long-term steady-state where the geologic carbon sources and sinks are in balance (see section 2.2).

We first evaluate the silicate weathering rate without incorporating feedbacks associated with CO_2 drawdown accompanying enhanced silicate weathering (see Table 2). In these experiments, we use a fixed *p*CO_2 (284.7 ppm) and calculate the total chemical weathering rate. With no SEAI, the global weathering rate (using the mean of the GEOCLIM results across the 573 parameter combinations) is 4.53 ± 0.04 Tmol/yr (95% confidence interval accounting for climate uncertainty) expressed as the total flux of Ca+Mg cations. The presence of flat SEAI land increases global weathering rate by ~5% to 4.76 ± 0.04 Tmol/yr; and the addition of topography increases it by another ~12%, to 5.32 ± 0.05 Tmol/yr. The overall weathering rate increase from the introduction of the SEAI is ~ 0.79 Tmol/yr at this fixed *p*CO_2 value with no carbon cycle feedbacks. Changes in the weathering flux with the introduction of the SEAI are concentrated over regions of topography (Figure 9a), and the topography contribution (~0.56 Tmol/yr or ~71%) provides the larger change as compared to the land area contribution (~0.23 Tmol/yr or ~29%; contrast Figure 9b to 9c). The 0.56 Tmol/yr topographic contribution arises from two mechanisms: directly through the steepness of topography and associated higher physical erosion rates which are parameterized as being dependent on slope and runoff, and indirectly through increased SEAI rainfall which also enhances fluxes of dissolved elements from chemical weathering profiles (Maher and Chamberlain, 2014). The former contributes ~67% of the 0.56 Tmol/yr increase, so the weathering flux increase related to the effects of enhanced rainfall on chemical weathering provides a smaller, but still significant, contribution.

Since tropical convection changes can alter global climate through teleconnections (Trenberth 1998), weathering flux changes resulting from SEAI topography could also occur outside of the SEAI. We find however that such changes are two orders of magnitude smaller than weathering changes over the SEAI: the difference in globally-integrated weathering flux between the modern SEAI and flat SEAI cases is ~0.56 Tmol/yr (Table 2), whereas the same difference in globally-integrated flux excluding the SEAI is only ~ -0.003 Tmol/yr (Table 2).

Hence, we confirm that the global weathering increase from the introduction of the SEAI originates almost entirely from changes to SEAI weathering. Our two findings – that (i) erosional effects contributes to the majority of the SEAI weathering increase from SEAI topography, and (ii) weathering changes outside the SEAI region are negligible as compared to the weathering changes over the SEAI land – are consistent with the interpretation that erosional effects of increased SEAI topography lead to significant and impactful changes in chemical weathering fluxes.

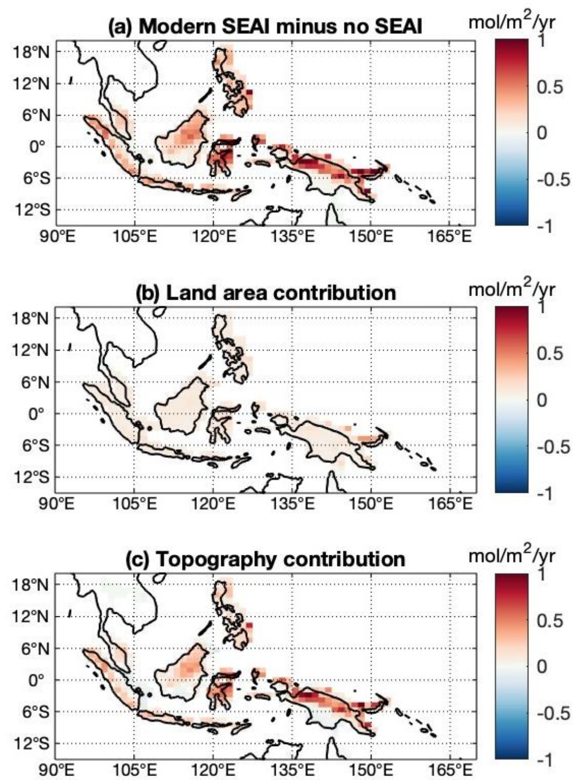

Figure 9. Change to the weathering flux with the presence of the SEAI. (a) Modern SEAI minus no SEAI; **(b)** land area contribution to (a), calculated as flat SEAI minus no SEAI; and **(c)** topography contribution, calculated as modern SEAI minus flat SEAI. The topography contribution provides the larger weathering change with the introduction of the SEAI (see Table 2). The weathering flux shown here is the mean over the 573 parameter combinations used in GEOCLIM. Differences are only plotted if significant at the 5% level (two-sided t-test) relative to the climate uncertainty.

If the global climate is allowed to reach carbon and energy equilibrium, the increased weathering flux from the presence of the SEAI would appreciably decrease steady-state atmospheric pCO_2 and global mean surface temperature (Table 2). We estimate atmospheric pCO_2 change to reach this new steady-state by estimating the CO_2 level at which volcanic degassing balances silicate weathering, and thus the resulting global mean temperature change (see section 2.2). In the no SEAI case, the model achieves an equilibrium pCO_2 of 439.1 ± 10.2 ppm and global mean surface temperature of 17.19 ± 0.12 ºC; this pCO_2 value is within the range postulated for the early Pliocene ca. 5 Ma (Beerling and Royer 2011). Introducing a flat SEAI decreases the equilibrium pCO_2 by ~45 ppm to 394.1 ± 7.7 ppm and global mean surface temperature by 0.64 ºC to 16.55 ± 0.11 ºC, approaching but not yet close to preindustrial levels. Introducing modern SEAI topography decreases the equilibrium pCO_2 by another ~109 ppm to 284.7 ppm, and global mean surface temperature by another 1.67 ºC to 14.88 ± 0.02 ºC. Thus, the introduction of SEAI topography (as opposed to land area) contributes to the majority of equilibrium pCO_2 and global mean surface temperature decrease.

The reduction of equilibrium atmospheric pCO_2 from the introduction of SEAI topography likely also contributes to an intensification of the zonal overturning circulation in addition to the direct effect from SEAI topography, following studies that argue for its weakening under global warming (Held and Soden 2006, Vecchi and Soden 2007). To examine such changes in circulation, we ran an additional fully-coupled simulation with flat SEAI and pCO_2 set to 394.1 ppm, which is the equilibrium pCO_2 found for the slab ocean flat SEAI case above. The zonal overturning circulation is indeed enhanced with the pCO_2 decrease for both the Indian and Pacific sectors (compare Figure 6c to Figure 6b), with increased subsidence over the eastern equatorial Pacific and western equatorial Indian/eastern equatorial Africa and further reduced rainfall (Figure 6d, red line). Accounting for the effect on equilibrium pCO_2, uplift over the SEAI region now increases by 19.4% compared to 13.5% if the pCO_2 change is not considered (Figure 7).

While we choose the mean value across the 573 GEOCLIM parameter combinations as our best estimate of the global weathering rate, there is a dependence of our results on the parameter combination chosen. However, for all parameter combinations the difference in the weathering rate between modern SEAI and no SEAI (the former minus the latter) is positive even if accounting for the climate uncertainty (Figure S6a); in other words, under any parameter combination the introduction of the SEAI increases the global weathering rate. This result also holds for the difference between modern SEAI and flat SEAI (Figure S6b), and between flat SEAI and no SEAI (Figure S6c).

6. Summary and Discussion

6.1 Summary of findings

Using simulations of an Earth System model (CESM1.2) in both slab ocean and fully-coupled configurations, we show that the presence of modern SEAI topography significantly increases rainfall over the SEAI (relative to a flat SEAI), and the zonal overturning circulation over the Indo-Pacific is enhanced with the help of dynamical ocean-atmosphere feedbacks, more strongly over the tropical Indian Ocean. The prominent role of SEAI topography contrasts with previous literature that typically associates these effects to the SEAI land surface area (Dayem et al. 2007, MC15).

Modern SEAI topography enhances rainfall over the SEAI region land by ~24% over that for flat SEAI, and concentrated over regions of high topography. Large-scale atmospheric uplift over the SEAI is increased, and the resulting zonal convergent flow introduces increased easterlies over the western equatorial Pacific and westerlies over the eastern equatorial Indian Ocean. The trade wind response induces a dynamical ocean-atmosphere feedback in both tropical ocean basins, such that the zonal overturning circulation over the Indo-Pacific sector is enhanced. However, the enhancement is modest, as atmospheric uplift over the SEAI region is increased only by ~14% including the dynamical ocean-atmosphere feedback. The enhancement is also not equal between basins: the zonal overturning circulation over the Indian Ocean is more strongly enhanced than the Walker circulation.

The presence of the SEAI enhances the global silicate weathering flux, leading to a decrease in atmospheric pCO_2 and global mean surface temperature. SEAI topography greatly enhances global weatherability, that is, the efficiency of the silicate weathering carbon sink for a given climatic state (François & Walker, 1992, Kump & Arthur, 1997, Penman et al., 2021). It does so largely through elevated physical erosion rates associated with the steeper topography, but also with a significant contribution from increased SEAI rainfall enhancing chemical weathering. At a fixed atmospheric pCO_2 level, the global weathering rate from the presence of the SEAI increases by ~0.79 Tmol/yr, of which ~71% is attributable to the topographic contribution. Allowing for atmospheric pCO_2 variation, the overall effect is that at energy and carbon equilibrium pCO_2 is lowered by ~154 ppm and ~2.31ºC, respectively, with topography contributing to the majority of the response (~109 ppm and ~1.67 ºC respectively). Our results support the hypothesis that the growth of SEAI topography over the last several million years have contributed to the global cooling and CO_2 drawdown in the late Miocene and Pliocene.

6.2 Geochemical considerations

It has been argued (Caves Rugenstein et al. 2021) that an enhancement in the silicate weathering flux from the SEAI relative to elsewhere on Earth, to the extent suggested by the weathering model GEOCLIM, is inconsistent with the Sr and Os isotope records. Understanding the drivers for the increase in ^{87}Sr/^{86}Sr values over the past 40 Ma is a problem of long-standing interest that is challenged by the non-uniqueness of interpretations including the effect of seafloor hydrothermal fluxes relative to continental weathering and regional variability in the composition of continental sources (e.g. Goddéris and Francois, 1995). Modeling the late Neogene marine Sr and Os isotopic composition is not feasible within the frame of this study since they reflect the evolution of global changes in weathering and mid-ocean ridge exchange, while we only investigate the sensitivity of weathering flux to changes in SEAI topography.

Nonetheless, some aspects of this issue can be addressed here. In the Caves Rugenstein et al. (2021) box model, the increasing ^{87}Sr/^{86}Sr values over the past 15 Ma are initially modeled to be due to an increasing flux of radiogenic Sr from the Himalaya—an increasing proportion of Sr with ^{87}Sr/^{86}Sr of 0.7214 (their Himalaya value) relative to an interpreted global mean riverine ^{87}Sr/^{86}Sr value of 0.710445 drives the increase. After fitting the data with this scenario, they then impose a flux associated with SEAI emergence under the assumption that all silicate weathering in the SEAI is from mafic lithologies which they assign a ^{87}Sr/^{86}Sr value of 0.7045. One problem with this approach is that it neglects the lithologic complexity of the region which includes clastic sedimentary rocks (Hartmann and Moosdorf, 2012), including those with provenance from ancient continental crust of Australia (Zimmermann and Hall, 2019) that have radiogenic ^{87}Sr/^{86}Sr values. Compiled ^{87}Sr/^{86}Sr measurements on bedrock arc lithologies from Indonesian islands, many of which are underlain by rifted fragments of Australian continental crust, give an average value of 0.7085 (Bayon et al., 2023). Similarly, riverine sediments from the Sepik River (New Guinea) have an average ^{87}Sr/^{86}Sr value of 0.7097 for clays and 0.7065 for silts (Bayon et al. 2021). Compared to the value of 0.7045 used by Caves Rugenstein et al. (2021), such higher values are a much smaller lever on global seawater values and can be consistent with the seawater record in the context of other evolving fluxes. Additional factors such as decreased hydrothermal fluxes that could accompany decreased seafloor spreading rate (Dalton et al., 2022) could also play a role in the upwards $^{87}Sr/^{86}Sr$ trend and complicate efforts to either invoke or rule out scenarios based on these data.

Similarly, modeling efforts assessing the effect of the emergence of SEAI on the Os isotope system also need to address the composition of what was eroded, which in the Central Range of New Guinea from Miocene to present was approximately half ophiolite and half sedimentary rock (Martin et al., 2023). Ophiolites tend to host unradiogenic Os isotope values with low Os concentrations, whereas sedimentary rocks commonly include fine-grained organic-rich units with more radiogenic Os isotope values with high Os concentrations (Peucker-Ehrenbrink and Ravizza, 2000). For example, Myrow et al. (2015) highlighted how the exhumation of a 150 m-thick Os-rich unit in the Himalaya with radiogenic ^{187}Os could have single-handedly driven the Neogene rise in Os isotope values. Consequently, the net effect of the Neogene rise of New Guinea on the Os isotope record is unclear. Overall, these considerations enable a late Neogene increase of SEAI weathering to be readily reconciled with isotopic records (Park et al. 2020).

Another caveat associated with the GEOCLIM results as pertains to changes in CO_2 levels is that they solely consider the inorganic carbon cycle. Associated with SEAI uplift there would also be: 1) the oxidation of petrographic organic carbon-rich rocks leading to CO_2 release (Zondervan et al., 2023); 2) the generation of sediment, particularly clays, that will bury new organic carbon in offshore basins where primary productivity is sustained by high local nutrient fluxes and thereby constitute a CO_2 sink (Murray and Jagoutz, 2024); and 3) the delivery of nutrient to the ocean that would foster bioproductivity and organic C burial (Hartmann et al., 2014). The balance between these processes associated with SEAI is unclear, such that the net effect is underconstrained. An important consideration is the need for stabilizing feedbacks associated with the consumption and release of oxygen associated with these processes (Maffre et al., 2021). Notably, ice core data over the past 800,000 years reveals oxygen cycles are within balance to a few percent (Stolper et al., 2016; Stolper et al., 2021). Stabilizing oxygen-mediated feedbacks in the organic carbon cycle between the magnitude of sources and sinks (Kump, 1989) would suggest the relative importance of the inorganic carbon cycle as modulating CO_2 concentrations.

6.3 Atmospheric circulation, rainfall, and weathering discussion

We contrast our results with MC15 who argued from empirical grounds for a connection between SEAI land area with the Walker circulation and sea surface temperatures over the eastern equatorial Pacific. According to MC15, a 60% increase in SEAI land area since 5 Ma proportionally increases rainfall over the SEAI region and the Walker circulation increases by ~6%; the enhanced trade winds were found to lead to a modest ~0.75ºC cooling over the eastern equatorial Pacific.

While we find a small enhancement of the Pacific Walker circulation in qualitative agreement with MC15, a somewhat larger enhancement occurs for the zonal overturning circulation over the tropical Indian Ocean. The tropical Indian response was not anticipated by MC15, but a number of recent papers investigating the response to paleoclimate forcings report a zonal response over the Indian Ocean (Dinezio and Tierney 2013, Dinezio et al. 2018, Du et al. 2023), suggesting that the tropical Indian Ocean is sensitive to climate forcings. DiNezio and Tierney (2013) report a sizable reduction to the Indo-Pacific Walker circulation with the exposure of the Sunda Shelf during the Last Glacial Maximum in the HadCM3 model, and with the larger reduction over the Indian Ocean sector. Their circulation response qualitatively resembles what we find with SEAI topography, but in the opposite direction (compare Figure 6b with Figure 4a of DiNezio and Tierney (2013)). The opposite response is interesting as the exposure of the Sunda and Sahul shelves substantially increases land area over the SEAI, which would argue for an increase to the zonal overturning circulation. One possibility is that the decrease in the ocean area might have resulted in a reduction of ocean heat flux convergence over the SEAI region and hence atmospheric uplift over the SEAI.

Paleoproxy studies have also shown a progressive aridification of East Africa since 3-4 million years ago (DeMenocal 1995, Cane and Molnar 2001). Our enhanced zonal overturning circulation in the Indian Ocean with SEAI topography and equilibrium pCO_2 change does lead to a drying over equatorial East Africa (Figure 6d, red line), suggesting an atmospheric mechanism for aridification that is linked to the emergence of SEAI topography and associated pCO_2 decrease. However, the simulated rainfall decrease over East Africa is small (~0.5mm/d), so additional influences are needed to explain the observed aridification over the last several million years. Possible mechanisms include changes to Indian Ocean SST resulting from the alteration of the Indonesian throughflow (Cane and Molnar 2001), the effect of tectonic uplift of eastern

African topography (Sepulchre et al. 2006), or complexities in the temperature-moisture relationship in the East African region (Baxter et al. 2023).

The equilibrium pCO_2 and global temperature changes in our simulations with no SEAI are somewhat smaller than the results of Park et al. (2020). The explanation does not arise from the contribution of SEAI to modern weathering flux, that is ~18.6% in our simulations that include Borneo and the Malay Peninsula, while Park et al. (2020) found a contribution of ~11.5% without. It rather comes from the climate sensitivity of the climate model they used (GFDL) being lower than that of the CESM1.2, and a more muted response of global weathering rate to global temperature with the GFDL than with the CESM. This means that, in our experiments, a smaller temperature change is required to compensate for the same perturbation of weathering rate, and a smaller pCO_2 change is necessary for the same global temperature change.

On the other hand, the change to global weathering and equilibrium pCO_2 found here are considerably larger than what was found in MC15. MC15 inferred a modest 19 ppm decrease in CO_2 concentrations and a 0.25ºC decrease in global mean temperature from a 60% increase in the SEAI land area (i.e., from approximately 60% to 100% of modern SEAI land area). We find instead a ~154 ppm and 2.31 ºC decrease from the introduction of the SEAI, with land area contributing ~45 ppm and ~0.64 ºC to the decrease and topography contributing ~109 ppm and ~1.67 ºC. The difference between MC15 and our study can be explained as follows. First, MC15 considered only a contribution from SEAI basalt weathering, estimated at 9% of the global weathering rate. Here, the weathering rate from the broader SEAI region, with all silicate lithological classes considered, is ~16% of the total weathering rate (Figure 9a). Secondly, MC15 considered a variation of 33% of the modern SEAI weathering flux (corresponding to an increase of land fraction from 60% to 100%, times a factor 5/6), whereas flattening the SEAI topography, in our experiments, reduces the SEAI weathering flux by ~70%. Finally, MC15 used a coefficient describing the exponential sensitivity of weathering to temperature $\alpha = 0.12\ K^{-1}$ (from Berner and Kothavala, 2001). An exponential fit of GEOCLIM simulations indicates a coefficient $\alpha = 0.07\ K^{-1}$, meaning a greater sensitivity of global mean temperature to variations of silicate weathering. The latter ($\alpha = 0.07\ K^{-1}$) is more likely in our opinion as it takes into account the limitation of weathering by erosion (supply-limited regime), which is not considered in the derivation of Berner & Kothavala (2001).

The differences between MC15 and our study also reflect the methodological differences. MC15 opted to make physical connections from empirical relationships and simple quantitative models, thus making the underlying assumptions explicit. The main weakness in our study is the uncertainty of the SEAI rainfall simulations given that (i) small islands and mountain ranges are not adequately resolved and (ii) convection is parameterized. Specifically, there is a question of whether global climate models with these limitations can adequately simulate the the enhancement of Maritime Continent rainfall by the presence of the islands (the so-called 'Island precipitation enhancement') as suggested by idealized cloud-resolving (Cronin et al. 2015) and regional convection-permitting models (Ruppert and Chen 2020); those studies find that diurnal mesoscale circulations to be critically important to island enhancement. The CESM1.2 rainfall also appears to be too sensitive to topography, given that seasonal cycle of rainfall has a dry bias over the western Maritime Continent where it is relatively flatter, and a wet bias over the eastern Maritime Continent where it is more mountainous (Figure S1); if this is true, then it implies that the change to rainfall, atmospheric uplift over the SEAI, and global weathering rate to SEAI topography may be overestimated.

On the other hand, the climate model offers a more reliable blueprint of large-scale atmospheric and ocean circulation changes and the underlying causal links, than relying on empirical relationships alone. Specifically, we question the appropriateness of the empirical connection made by Dayem et al. (2007) between SEAI rainfall and the Walker circulation; we suspect that the empirical connection is largely influenced by zonal shifts in the Walker circulation resulting from El Nino-Southern Oscillation changes; atmospheric convection that is usually centered over the SEAI shifts to the western equatorial Pacific during an El Niño, thus weakening the Walker circulation. However, the zonal overturning changes we find in our simulations do not arise from not zonal shifts, but rather that atmospheric convection is enhanced over the SEAI. Finding an adequate answer to our problem may thus require the use of global and coupled convection-permitting models.

Finally, we limited our analysis of the tropical large-scale circulation effects of the SEAI largely to the role of SEAI topography, leaving aside the more difficult question of the contribution of SEAI land area. How SEAI land affects the large-scale circulation depends on how one specifies the ocean that the SEAI replaces. For example, Zhang et al. (2019)'s 'NOLAND' simulation replaces their SEAI land surface with ocean by specifying sea surface temperatures extrapolated from the surrounding ocean using bilinear interpolation, unlike in this study where we use a slab ocean of 16 m depth and zero ocean heat flux convergence. The SEAI land contribution from our slab ocean simulations (Figure 3, left panels) shows a distinct semi-annual increase in the rainfall over land during the equinox seasons (MAM and SON). This semiannual response is largely absent in Zhang et al. (2019) (see their figure 5, NOLAND minus NOTOPO; the sign needs to be reversed to compare their results to ours). On the other hand, Zhang et al. (2019) get a large rainfall response over the ocean in the northwest quadrant of the SEAI region that is absent in our simulations. If SEAI changes were imposed on a dynamical ocean on the other hand, then one would need to specify the bathymetry, and the altered ocean currents would further change the Indo-Pacific climate, for example through altering the Indonesian throughflow (Cane and Molnar 2001). Regardless, our study demonstrates the significant role that tectonic changes in the SEAI have played to the regional climate over the Indo-Pacific and to global climate over that past 10 million years.

Acknowledgments

The research was supported by a National Science Foundation Frontier Research in Earth Science grant EAR-1925990 awarded to N.L.S.-H. and J.C.H.C, and National Science Foundation Frontier Research in Earth Science grant EAR-1926001 to F.A.M. We thank Quentin Nicolas and Min-Hui Lo for helpful discussions, and Gerrit Trapp-Müller, Arthur Oldeman and an anonymous reviewer for their detailed reviews. We dedicate this work to the memory of Peter Molnar, whose work and example inspires us all.

Open Research

CESM1.2 and GEOCLIM model input and data files used in this study are available through Chiang and Maffre (2023). The CESM 1.2 code used for the climate model simulations is available at https://www2.cesm.ucar.edu/models/cesm1.2/. The GEOCLIM code is available at Github via https://github.com/piermafrost/GEOCLIM-dynsoil-steady-state/tree/SEAI and permanently archived at Zenodo (Maffre et al. 2023).

References

Abbott, L.D., Silver, E.A., Thompson, P.R., Filewicz, M.V. and Schneider, C., 1994. Stratigraphic constraints on the development and timing of arc-continent collision in northern Papua New Guinea. *Journal of Sedimentary Research*, *64*(2b), pp.169-183.

Aiello, I.W., Bova, S.C., Holbourn, A.E., Kulhanek, D.K., Ravelo, A.C. and Rosenthal, Y., 2019. Climate, sea level and tectonic controls on sediment discharge from the Sepik River, Papua New Guinea during the Mid-to Late Pleistocene. *Marine Geology*, *415*, p.105954.

Bayon, G., Freslon, N., Germain, Y., Bindeman, I.N., Trinquier, A. and Barrat, J.A., 2021. A global survey of radiogenic strontium isotopes in river sediments. *Chemical Geology*, *559*, p.119958.

Bayon, G., Patriat, M., Godderis, Y., Trinquier, A., De Deckker, P., Kulhanek, D.K., Holbourn, A. and Rosenthal, Y., 2023. Accelerated mafic weathering in Southeast Asia linked to late Neogene cooling. *Science Advances*, *9*(13), p.eadf3141.

Baxter, A.J., Verschuren, D., Peterse, F., Miralles, D.G., Martin-Jones, C.M., Maitituerdi, A., Van der Meeren, T., Van Daele, M., Lane, C.S., Haug, G.H. and Olago, D.O., 2023. Reversed Holocene temperature–moisture relationship in the Horn of Africa. *Nature, 620(7973)*, pp.336-343.

Beerling, D.J. and Royer, D.L., 2011. Convergent Cenozoic CO2 history. *Nature geoscience*, *4*(7), pp.418-420.

Berner, R.A. and Caldeira, K., 1997. The need for mass balance and feedback in the geochemical carbon cycle. *Geology*, *25*(10), pp.955-956.

Berner, R.A. and Kothavala, Z., 2001. GEOCARB III: a revised model of atmospheric CO2 over Phanerozoic time. *American Journal of Science*, *301*(2), pp.182-204.

Biasutti, M., Yuter, S.E., Burleyson, C.D. and Sobel, A.H., 2012. Very high resolution rainfall patterns measured by TRMM precipitation radar: Seasonal and diurnal cycles. *Climate dynamics*, *39*, pp.239-258.

Biasutti, M., Voigt, A., Boos, W.R., Braconnot, P., Hargreaves, J.C., Harrison, S.P., Kang, S.M., Mapes, B.E., Scheff, J., Schumacher, C. and Sobel, A.H., 2018. Global energetics and local physics as drivers of past, present and future monsoons. *Nature Geoscience*, *11*(6), pp.392-400.

Bjerknes, J., 1969. Atmospheric teleconnections from the equatorial Pacific. *Monthly weather review*, *97*(3), pp.163-172.

Cane, M.A. and Molnar, P., 2001. Closing of the Indonesian seaway as a precursor to east African aridification around 3–4 million years ago. *Nature*, *411*(6834), pp.157-162.

Caves Rugenstein, J.K., Ibarra, D.E., Zhang, S., Planavsky, N.J. and von Blanckenburg, F., 2021. Isotope mass-balance constraints preclude that mafic weathering drove Neogene cooling. *Proceedings of the National Academy of Sciences*, *118*(30), p.e2026345118.

Chang, C.P., Wang, Z., McBride, J. and Liu, C.H., 2005. Annual cycle of Southeast Asia—Maritime Continent rainfall and the asymmetric monsoon transition. *Journal of climate*, *18*(2), pp.287-301.

Chang, P., Zhang, S., Danabasoglu, G., Yeager, S.G., Fu, H., Wang, H., Castruccio, F.S., Chen, Y., Edwards, J., Fu, D. and Jia, Y., 2020. An unprecedented set of high-resolution earth system simulations for understanding multiscale interactions in climate variability and change. *Journal of Advances in Modeling Earth Systems*, *12*(12), p.e2020MS002298.

Chen, C.C., Lo, M.H., Im, E.S., Yu, J.Y., Liang, Y.C., Chen, W.T., Tang, I., Lan, C.W., Wu, R.J. and Chien, R.Y., 2019. Thermodynamic and dynamic responses to deforestation in the Maritime Continent: a modeling study. *Journal of Climate*, *32*(12), pp.3505-3527.

Chiang, J.C.H., and Maffre, P., 2023. Data from: The role of Southeast Asian Island topography on Indo-Pacific climate and silicate weathering [Dataset]. Dryad. https://doi.org/10.6078/D1271P

Cottam, M.A., Hall, R., Sperber, C., Kohn, B.P., Forster, M.A. and Batt, G.E., 2013. Neogene rock uplift and erosion in northern Borneo: evidence from the Kinabalu granite, Mount Kinabalu. *Journal of the Geological Society*, *170*(5), pp.805-816.

Cronin, T.W., Emanuel, K.A. and Molnar, P., 2015. Island precipitation enhancement and the diurnal cycle in radiative-convective equilibrium. *Quarterly Journal of the Royal Meteorological Society*, *141*(689), pp.1017-1034.

Crowhurst, P.V., Hill, K.C., Foster, D.A. and Bennett, A.P., 1996. Thermochronological and geochemical constraints on the tectonic evolution of northern Papua New Guinea. *Geological Society, London, Special Publications*, *106*(1), pp.525-537.

Dalton, C.A., Wilson, D.S. and Herbert, T.D., 2022. Evidence for a global slowdown in seafloor spreading since 15 Ma. *Geophysical Research Letters*, *49*(6), p.e2022GL097937.

Dayem, K.E., Noone, D.C. and Molnar, P., 2007. Tropical western Pacific warm pool and maritime continent precipitation rates and their contrasting relationships with the Walker Circulation. *Journal of Geophysical Research: Atmospheres*, *112*(D6).

Dee, D.P., Uppala, S.M., Simmons, A.J., Berrisford, P., Poli, P., Kobayashi, S., Andrae, U., Balmaseda, M.A., Balsamo, G., Bauer, D.P. and Bechtold, P., 2011. The ERA‐Interim reanalysis: Configuration and performance of the data assimilation system. *Quarterly Journal of the royal meteorological society*, *137*(656), pp.553-597.

Demenocal, P.B., 1995. Plio-pleistocene African climate. *Science*, *270*(5233), pp.53-59.

DiNezio, P.N. and Tierney, J.E., 2013. The effect of sea level on glacial Indo-Pacific climate. *Nature Geoscience*, *6*(6), pp.485-491.

DiNezio, P.N., Tierney, J.E., Otto-Bliesner, B.L., Timmermann, A., Bhattacharya, T., Rosenbloom, N. and Brady, E., 2018. Glacial changes in tropical climate amplified by the Indian Ocean. *Science Advances*, *4*(12), p.eaat9658.

Donnadieu, Y., Goddéris, Y., Ramstein, G., Nédélec, A. and Meert, J., 2004. A 'snowball Earth' climate triggered by continental break-up through changes in runoff. *Nature*, *428*(6980), pp.303-306.

Du, X., Russell, J.M., Liu, Z., Otto-Bliesner, B.L., Oppo, D.W., Mohtadi, M., Zhu, C., Galy, V.V., Schefuß, E., Yan, Y. and Rosenthal, Y., 2023. North Atlantic cooling triggered a zonal mode over the Indian Ocean during Heinrich Stadial 1. *Science Advances*, *9*(1), p.eadd4909.

Fedorov, A.V. and Philander, S.G., 2001. A stability analysis of tropical ocean–atmosphere interactions: Bridging measurements and theory for El Niño. *Journal of Climate*, *14*(14), pp.3086-3101.

Francois, L.M. and Walker, J.C., 1992. Modelling the Phanerozoic carbon cycle and climate; constraints from the 87 Sr/86 Sr isotopic ratio of seawater. *American Journal of Science*, *292*(2), pp.81-135.

Gabet, E.J. and Mudd, S.M., 2009. A theoretical model coupling chemical weathering rates with denudation rates. *Geology*, *37*(2), pp.151-154.

Gill, A.E., 1980. Some simple solutions for heat‐induced tropical circulation. *Quarterly Journal of the Royal Meteorological Society*, *106*(449), pp.447-462.

Goddéris, Y., Donnadieu, Y., Carretier, S., Aretz, M., Dera, G., Macouin, M. and Regard, V., 2017. Onset and ending of the late Palaeozoic ice age triggered by tectonically paced rock weathering. *Nature Geoscience*, *10*(5), pp.382-386.

Goddéris, Y. and François, L.M., 1995. The Cenozoic evolution of the strontium and carbon cycles: relative importance of continental erosion and mantle exchanges. *Chemical Geology*, *126*(2), pp.169-190.

Hall, R., 2017. Southeast Asia: New views of the geology of the Malay Archipelago. *Annual Review of Earth and Planetary Sciences*, *45*, pp.331-358.

Hartmann, J. and Moosdorf, N., 2012. The new global lithological map database GLiM: A representation of rock properties at the Earth surface. *Geochemistry, Geophysics, Geosystems*, *13*(12).

Hartmann, J., Moosdorf, N., Lauerwald, R., Hinderer, M. and West, A.J., 2014. Global chemical weathering and associated P-release—The role of lithology, temperature and soil properties. *Chemical Geology*, *363*, pp.145-163.

Held, I.M. and Soden, B.J., 2006. Robust responses of the hydrological cycle to global warming. *Journal of climate*, *19*(21), pp.5686-5699.

Hennig, J., Hall, R., Forster, M.A., Kohn, B.P. and Lister, G.S., 2017. Rapid cooling and exhumation as a consequence of extension and crustal thinning: Inferences from the Late Miocene to Pliocene Palu Metamorphic Complex, Sulawesi, Indonesia. *Tectonophysics*, *712*, pp.600-622.

Hersbach, H., Bell, B., Berrisford, P., Hirahara, S., Horányi, A., Muñoz-Sabater, J., Nicolas, J., Peubey, C., Radu, R., Schepers, D. and Simmons, A., 2020. The ERA5 global reanalysis. *Quarterly Journal of the Royal Meteorological Society*, *146*(730), pp.1999-2049.

Hill, K.C. and Gleadow, A.J.W., 1989. Uplift and thermal history of the Papuan Fold Belt, Papua New Guinea: Apatite fission track analysis. *Australian Journal of Earth Sciences*, *36*(4), pp.515-539.

Hilton, R.G. and West, A.J., 2020. Mountains, erosion and the carbon cycle. Nature Reviews Earth & Environment, 1(6), pp.284-299.

Huffman, G.J., Bolvin, D.T., Nelkin, E.J., Wolff, D.B., Adler, R.F., Gu, G., Hong, Y., Bowman, K.P. and Stocker, E.F., 2007. The TRMM multisatellite precipitation analysis (TMPA):

Quasi-global, multiyear, combined-sensor precipitation estimates at fine scales. *Journal of hydrometeorology*, *8*(1), pp.38-55.

Hurrell, J.W., Holland, M.M., Gent, P.R., Ghan, S., Kay, J.E., Kushner, P.J., Lamarque, J.F., Large, W.G., Lawrence, D., Lindsay, K. and Lipscomb, W.H., 2013. The community earth system model: a framework for collaborative research. *Bulletin of the American Meteorological Society*, *94*(9), pp.1339-1360.

Huybers, P. and Molnar, P., 2007. Tropical cooling and the onset of North American glaciation. *Climate of the Past*, *3*(3), pp.549-557.

Kumar, K.K., Rajagopalan, B. and Cane, M.A., 1999. On the weakening relationship between the Indian monsoon and ENSO. *Science*, *284*(5423), pp.2156-2159.

Kump, L.R. and Arthur, M.A., 1997. Global chemical erosion during the Cenozoic: Weatherability balances the budgets. In *Tectonic uplift and climate change* (pp. 399-426). Boston, MA: Springer US.

Kump, L.R. (1989). Chemical stability of the atmosphere and ocean. Global and Planetary Change, 1(1–2), 123-136. https://doi.org/10.1016/0921-8181(89)90019-2.

Le Hir, G., Donnadieu, Y., Goddéris, Y., Meyer-Berthaud, B., Ramstein, G. and Blakey, R.C., 2011. The climate change caused by the land plant invasion in the Devonian. *Earth and Planetary Science Letters*, *310*(3-4), pp.203-212.

Liberti, G.L., Chéruy, F. and Desbois, M., 2001. Land effect on the diurnal cycle of clouds over the TOGA COARE area, as observed from GMS IR data. *Monthly weather review*, *129*(6), pp.1500-1517.

Maffre, P., Ladant, J.B., Moquet, J.S., Carretier, S., Labat, D. and Goddéris, Y., 2018. Mountain ranges, climate and weathering. Do orogens strengthen or weaken the silicate weathering carbon sink?. *Earth and Planetary Science Letters*, *493*, pp.174-185.

Maffre, P., Swanson-Hysell, N.L. and Goddéris, Y., 2021. Limited carbon cycle response to increased sulfide weathering due to oxygen feedback. Geophysical Research Letters, 48(19), p.e2021GL094589

Maffre, P., Chiang, J.C.H. and Swanson-Hysell, N.L., 2023. The effect of the Pliocene temperature pattern on silicate weathering and Pliocene–Pleistocene cooling. *Climate of the Past*, *19*(7), pp.1461-1479.

Maffre, P., Swanson-Hysell, N., hematite-berkeley, & Park, Y. (2023). piermafrost/GEOCLIM-dynsoil-steady-state: version 2.0 compatible with Chiang et al. (submitted to Paleoceanogr. Paleoclimatol.) [Software]. Zenodo. https://doi.org/10.5281/zenodo.10260279

Maher, K. and Chamberlain, C.P., 2014. Hydrologic regulation of chemical weathering and the geologic carbon cycle. *science*, *343*(6178), pp.1502-1504.

Marcilly, C.M., Maffre, P., Le Hir, G., Pohl, A., Fluteau, F., Goddéris, Y., Donnadieu, Y., Heimdal, T.H. and Torsvik, T.H., 2022. Understanding the early Paleozoic carbon cycle balance and climate change from modelling. *Earth and Planetary Science Letters*, *594*, p.117717.

Martin, P.E., Macdonald, F.A., McQuarrie, N., Flowers, R.M. and Maffre, P.J., 2023. The rise of New Guinea and the fall of Neogene global temperatures. *Proceedings of the National Academy of Sciences*, *120*(40), p.e2306492120

Molnar, P. and Cane, M.A., 2002. El Niño's tropical climate and teleconnections as a blueprint for pre-Ice Age climates. *Paleoceanography*, *17*(2), pp.11-1 - 11-11.

Molnar, P. and Cronin, T.W., 2015. Growth of the Maritime Continent and its possible contribution to recurring Ice Ages. *Paleoceanography*, *30*(3), pp.196-225.

Murray, J., & Jagoutz, O. (2024). Palaeozoic cooling modulated by ophiolite weathering through organic carbon preservation. Nat. Geosci., 17, 88–93. https://doi.org/10.1038/s41561-023-01342-9

Myrow, P.M., Hughes, N.C., Derry, L.A., McKenzie, N.R., Jiang, G., Webb, A.A.G., Banerjee, D.M., Paulsen, T.S., & Singh, B.P. (2015). Neogene marine isotopic evolution and the erosion of Lesser Himalayan strata: Implications for Cenozoic tectonic history. Earth and Planetary Science Letters, 417, 142-150. https://doi.org/10.1016/j.epsl.2015.02.016.

Nicolas, Q. and Boos, W.R., 2022. A theory for the response of tropical moist convection to mechanical orographic forcing. *Journal of the Atmospheric Sciences*, *79*(7), pp.1761-1779.

Park, Y., Maffre, P., Goddéris, Y., Macdonald, F.A., Anttila, E.S. and Swanson-Hysell, N.L., 2020. Emergence of the Southeast Asian islands as a driver for Neogene cooling. *Proceedings of the National Academy of Sciences*, *117*(41), pp.25319-25326.

Penman, D.E., Rugenstein, J.K.C., Ibarra, D.E. and Winnick, M.J., 2020. Silicate weathering as a feedback and forcing in Earth's climate and carbon cycle. *Earth-Science Reviews*, *209*, p.103298.

Peucker-Ehrenbrink, B. and Ravizza, G., 2000. The marine osmium isotope record. *Terra Nova*, *12*(5), pp.205-219.

Ramage, C.S., 1968. Role of a tropical "maritime continent" in the atmospheric circulation. *Monthly Weather Review*, *96*(6), pp.365-370.

Ren, X., Lunt, D.J., Hendy, E., von der Heydt, A., Abe-Ouchi, A., Otto-Bliesner, B.L., Williams, C.J., Stepanek, C., Guo, C., Chandan, D. and Lohmann, G., 2022. The hydrological cycle and ocean circulation of the Maritime Continent in the mid-Pliocene: results from PlioMIP2. *EGUsphere*, *2022*, pp.1-41.

Robertson, A.W., Moron, V., Qian, J.H., Chang, C.P., Tangang, F., Aldrian, E., KOH, T.Y. and Liew, J., 2011. The maritime continent monsoon. *The global monsoon system: research and forecast*, pp.85-98.

Ruppert Jr, J.H. and Chen, X., 2020. Island rainfall enhancement in the Maritime Continent. *Geophysical Research Letters*, *47*(5), p.e2019GL086545.

Sato, T., Miura, H., Satoh, M., Takayabu, Y.N. and Wang, Y., 2009. Diurnal cycle of precipitation in the tropics simulated in a global cloud-resolving model. *Journal of Climate*, *22*(18), pp.4809-4826.

Sepulchre, P., Ramstein, G., Fluteau, F., Schuster, M., Tiercelin, J.J. and Brunet, M., 2006. Tectonic uplift and Eastern Africa aridification. *Science*, *313*(5792), pp.1419-1423.

Siever, R., 1968. Sedimentalogical consequences of a steady-state ocean-atmosphere. *Sedimentology*, *11*(1-2), pp.5-29.

Sobel, A.H., Burleyson, C.D. and Yuter, S.E., 2011. Rain on small tropical islands. *Journal of Geophysical Research: Atmospheres*, *116*(D8).

Stolper, D.A., & Keller, C. (2018). A record of deep-ocean dissolved O2 from the oxidation state of iron in submarine basalts. Nature, 553, 323–327. https://doi.org/10.1038/nature25009

Stolper, D.A., Higgins, J.A., & Derry, L.A. (2021). The role of the solid earth in regulating atmospheric O2 levels. American Journal of Science, 321(10), 1381-1444. https://doi.org/10.2475/10.2021.01

Tate, G.W., McQuarrie, N., van Hinsbergen, D.J., Bakker, R.R., Harris, R. and Jiang, H., 2015. Australia going down under: Quantifying continental subduction during arc-continent accretion in Timor-Leste. *Geosphere*, *11*(6), pp.1860-1883.

Trenberth, K.E., Branstator, G.W., Karoly, D., Kumar, A., Lau, N.C. and Ropelewski, C., 1998. Progress during TOGA in understanding and modeling global teleconnections associated with tropical sea surface temperatures. *Journal of Geophysical Research: Oceans*, *103*(C7), pp.14291-14324.Webb, M., White, L.T., Jost, B.M. and Tiranda, H., 2019. The Tamrau Block of NW New Guinea records late Miocene–Pliocene collision at the northern tip of the Australian Plate. *Journal of Asian Earth Sciences*, *179*, pp.238-260.

Vecchi, G.A. and Soden, B.J., 2007. Global warming and the weakening of the tropical circulation. *Journal of Climate*, *20*(17), pp.4316-4340.

Vizcaíno, M., Rupper, S. and Chiang, J.C.H., 2010. Permanent El Niño and the onset of Northern Hemisphere glaciations: Mechanism and comparison with other hypotheses. *Paleoceanography*, *25*(2).

Walker, J.C., Hays, P.B. and Kasting, J.F., 1981. A negative feedback mechanism for the long-term stabilization of Earth's surface temperature. *Journal of Geophysical Research: Oceans*, *86*(C10), pp.9776-9782.

Weiland Jr, R.J., 1999. *Emplacement of the Irian ophiolite and unroofing of the Ruffaer metamorphic belt of Irian Jaya, Indonesia*. The University of Texas at Austin.

Weiland, R.J. and Cloos, M., 1996. Pliocene-Pleistocene asymmetric unroofing of the Irian fold belt, Irian Jaya, Indonesia: Apatite fission-track thermochronology. *Geological Society of America Bulletin*, *108*(11), pp.1438-1449.

West, A.J., 2012. Thickness of the chemical weathering zone and implications for erosional and climatic drivers of weathering and for carbon-cycle feedbacks. *Geology*, *40*(9), pp.811-814.

Xie, S.P., Xu, H., Saji, N.H., Wang, Y. and Liu, W.T., 2006. Role of narrow mountains in large-scale organization of Asian monsoon convection. *Journal of climate*, *19*(14), pp.3420-3429.

Zeng, N. and Neelin, J.D., 1999. A land–atmosphere interaction theory for the tropical deforestation problem. *Journal of Climate*, *12*(3), pp.857-872.

Zhang, T., Shao, X. and Li, S., 2017. Impacts of atmospheric processes on ENSO asymmetry: A comparison between CESM1 and CCSM4. *Journal of Climate*, *30*(23), pp.9743-9762.

Zhang, T., Tam, C.Y., Jiang, X., Yang, S., Lau, N.C., Chen, J. and Laohalertchai, C., 2019. Roles of land-surface properties and terrains on Maritime Continent rainfall and its seasonal evolution. *Climate Dynamics*, *53*, pp.6681-6697.

Zhou, L. and Wang, Y., 2006. Tropical Rainfall Measuring Mission observation and regional model study of precipitation diurnal cycle in the New Guinean region. *Journal of Geophysical Research: Atmospheres*, *111*(D17).

Zimmermann, S. and Hall, R., 2019. Provenance of Cretaceous sandstones in the Banda Arc and their tectonic significance. *Gondwana Research*, *67*, pp.1-20.

Zondervan, J.R., Hilton, R.G., Dellinger, M., et al. (2023). Rock organic carbon oxidation CO2 release offsets silicate weathering sink. Nature, 623, 329–333. https://doi.org/10.1038/s41586-023-06581-9

Name of simulation	**Description**	**Slab ocean**	**Fully coupled**
No SEAI	Land identified as part of SEAI (see Figure 1) is removed and replaced with a slab ocean of 16 m depth and zero ocean heat flux convergence.	yes	no
0% SEAI topography **(aka flat SEAI)**	Topography over SEAI is set to zero	yes	yes
50% SEAI topography	Topography over SEAI is set to 50% of modern height	yes	yes
100% SEAI topography **(aka modern SEAI)**	Topography over SEAI is set to modern height. This is also the CESM1.2 preindustrial (PI) control run	yes	yes
150% SEAI topography	Topography over SEAI is set to 150% of modern height	yes	yes
Flat SEAI & 394ppm	Same as flat SEAI but pCO_2 set to 394.1ppm	no	yes

Table 1. Names and descriptions of the key CESM1.2 simulations used in this paper. Slab ocean simulations are 70 years long with the last 30 years used for the analysis. Fully coupled simulations are 110 years long with the last 70 years used for the analysis. All runs are done with a preindustrial pCO_2 level of 284.7ppm except where indicated. For the No SEAI and flat SEAI cases with slab ocean, an additional double CO_2 (569.4 ppm) simulation was done for working out the equilibrium CO_2 and global mean surface temperature resulting from the modified weathering (see section 2.2). For the no SEAI case, we additionally simulated two cases: one where the slab ocean depth over the SEAI gridpoints is doubled to 32m, and the other where the ocean heat flux convergence over the SEAI gridpoints is set to 20 W/m^2 (from 0 W/m^2). These runs were used to test the sensitivity of our results to the specification of said properties of the slab ocean.

	No SEAI	**Flat SEAI**	**Modern SEAI**
Global weathering rate (Tmol/yr) at *p*CO_2 = 284.7ppm	4.53 ± 0.04	4.76 ± 0.04	5.32 ± 0.05
Global weathering rate excluding SEAI (Tmol/yr) at *p*CO_2 = 284.7ppm	4.53 ± 0.04	4.51 ± 0.04	4.48 ± 0.04
***p*CO_2 (ppm) at equilibrium**	439.1 ± 10.2	394.1 ± 7.7	284.7
GMST (ºC) at equilibrium	17.19 ± 0.12	16.55 ± 0.11	14.88 ± 0.02

Table 2. Results from the climate-silicate weathering model with varying SEAI. (Top row) Global weathering rate at fixed pCO_2 (284.7ppm). **(middle row)** Atmospheric *p*CO_2 at equilibrium. **(bottom row)** Global mean surface temperature (GMST) at equilibrium. The modern SEAI simulation provides the *p*CO_2 and GMST baselines, so there is no uncertainty associated with them. Values of weathering rate reported are for the mean across the 573 GEOCLIM parameter combinations, and the range indicate the 95% confidence interval associated with the climate uncertainty, expressed as ± 1.96 times the standard error of the 30-yr sampled climate data.